Intermetallics 19 (2011) 267–275

Contents lists available at ScienceDirect

Intermetallics

journal homepage: www.elsevier.com/locate/intermet

The evolution of the microstructure in amorphous $Al_{85}Ce_8Ni_5Co_2$ alloy during heat treatment and severe plastic deformation: A comparative study

P. Henits [a,*], Á. Révész [a], L.K. Varga [b], Zs. Kovács [a,c]

[a] Department of Materials Physics, Eötvös University, Budapest H-1518, P.O.B. 32, Budapest, Hungary
[b] Research Institute for Solid state Physics and Optics, Hungarian Academy of Sciences, H-1525 Budapest, P.O.B. 49, Hungary
[c] School of Electrical, Electronic & Mechanical Engineering, University College Dublin, Belfield, Dublin 4, Ireland

ARTICLE INFO

Article history:
Received 22 June 2009
Received in revised form
30 August 2010
Accepted 6 October 2010
Available online 1 November 2010

Keywords:
B. Glasses, metallic
B. Thermal stability
C. Nanocrystals
D. Microstructure
E. Phase stability, prediction

ABSTRACT

The effect of three different devitrification routes, i.e. isothermal heat treatment, high pressure torsion and ball milling of amorphous $Al_{85}Ce_8Ni_5Co_2$ alloy have been studied systematically. The phase selection during the different crystallization sequences is explained by different thermodynamic barriers and growth rates. Low temperature heat treatment results in the formation of α-Al and a metastable phase (φ). Although, the nucleation of $Al_{11}Ce_3$ phase is also likely in this temperature range, the lack of its growth is explained by kinetic considerations. Ball milling results in the formation of the stable phase mixture (α-Al and $Al_{11}Ce_3$). This process can be considered as a high temperature heat treatment at intermediate pressures (<2 GPa). High pressure torsion at the applied pressure of 6 GPa results in the primary formation of α-Al nanocrystals.

1. Introduction

Devitrification of metallic glasses can be attained either by thermal activation or by mechanical deformation. Each process changes the initial metastable state of amorphous alloy in a different way. Typically, thermally-induced crystallization is a homogenous process with negligible thermal gradients. On the other hand, deformation can induce large gradients below the glass transition temperature (T_g), i.e. highly localized shear bands at high stress levels, affecting only a very tiny volume fraction of the sample which can lead to catastrophic failures [1–3]. As Lewandowski and Greer have shown, the temperature rise during this softening process can be as high as a few thousand K over a few nanoseconds [4].

Metallic glasses are ideal model systems for the investigation of nucleation and growth on nano-scale, because of the relatively sluggish atomic rearrangements near T_g. In the last decades several nucleation models have been proposed to describe the crystallization mechanism of metallic glasses via thermal activation [5], however, the detailed mechanism of deformation induced crystallization is still the subject of considerable debate.

According to the classical theory of crystal growth in metastable supercooled liquid, the growth rate of the crystal is described by the thermodynamic driving force for crystallization and material transport [6]. The former is given by the difference in the free energy between liquid and crystal, whereas the latter is determined by the translational diffusion constant.

Under applied external stress the changes in the thermodynamic driving force and in the atomic mobility have to be taken into account. In the view of the classical nucleation theory the free energy change must be supplemented with a term proportional to the plastic work [7]. The atomic transport can be treated in the frame of free volume approximation [8], under thermal treatment just the annihilation of free volume occurs resulting in densification, i.e. relaxation without crystallization, while under plastic deformation the generation of free volume takes place via a dynamic equilibrium between creation and annihilation [8,9], assuring enough mobility for the crystallization and for the further growth of the emerging nuclei.

Recent experimental reviews have shown that deformation induced crystallization is a common phenomena of metallic glasses [10–19]. Focusing on Al-based metallic glasses, studies deal with the influence of composition, temperature rise and stress state on the nucleation of crystalline phases. According to their first crystallization step and the corresponding crystalline

* Corresponding author. Tel.: +36 1 372 2845; fax: +36 1 372 2811.
E-mail address: henits@metal.elte.hu (P. Henits).

0966-9795/$ – see front matter © 2010 Elsevier Ltd. All rights reserved.
doi:10.1016/j.intermet.2010.10.007

products Al-based metallic glasses can be classified into several groups. For instance, in the $Al_{90}Fe_5Gd_5$, $Al_{90}Fe_5Ce_5$, $Al_{85}Nd_8Ni_5Co_2$ and $Al_{85}Y_8Ni_5Co_2$ systems, where the first crystallization event is the precipitation of α-Al, the deformation promotes the nucleation of α-Al [2,20–22]. The diffusion profile around Al precipitates in the $Al_{90}Fe_5Gd_5$ amorphous alloy after deformation is nearly identical to that of obtained after isothermal heat treatments, suggesting significant temperature rise as a consequence of deformation [23]. The observed α-Al nanocrystals induced by deformation usually locates in the vicinity of shear bands, therefore one could assume that the temperature rise and the atomic mobility in the shear band trigger the nucleation. However, as Demetriou and Johnson have pointed out that solely temperature rise cannot explain the crystallization, because the driving force for nucleation decreases with increasing temperature [24].

On contrary, just a few works are concerned with non-primary crystallizing alloys. In amorphous $Al_{85}Ni_{10}Ce_5$ (crystallization begins with the simultaneous nucleation of α-Al and two intermetallic compounds [25]) no detectable crystallization has been observed after prolonged ball milling [2]. More interestingly, applying extremely large deformation we have reported primary crystallization of α-Al nanocrystals in a thermally eutectic-like crystallizing $Al_{85}Ce_8Ni_5Co_2$ amorphous alloy [26,27].

In this work a comparative study has been carried out on the crystallization of $Al_{85}Ce_8Ni_5Co_2$ metallic glass attained either by thermal treatment or by severe plastic deformation applying high pressure torsion (HPT) and ball milling (BM). HPT was originally invented for producing highly dense, bulk ultrafine-grained (submicron-grain-sized or nanostructured) materials [28]. However, HPT can successfully be applied to produce massive samples from melt-quenched amorphous ribbons by consolidation at room temperature [26,27,29–32]. In order to explain the differences between the crystallization routes and evaluate the working conditions during heat treatments, HPT and BM, both thermodynamic and kinetic aspects of nucleation and growth of the emerging phases will be discussed.

2. Experimental

2.1. Sample preparation

Ingot of $Al_{85}Ce_8Ni_5Co_2$ was synthesized by induction melting of a mixture of high purity (99.9%) Al, Ce, Ni and Co metals. Fully amorphous ribbon sample was obtained using a single roller melt spinning technique in inert atmosphere.

Some portion of the as-quenched ribbon was cut into small pieces (flakes) and then placed between anvils of the HPT device. The shear deformation was performed by subjecting the flake to five whole rotations under hydrostatic pressure of 6 GPa. The HPT process results in several porosity free disks with a diameter of 10 mm and thickness of about 120 μm. As was shown, the amount of plastic strain increases linearly with the distance measured from the torsion axis [33]. In order to investigate the radial dependence of the microstructure and thermal properties the HPT disk was fragmented into small pieces and systematically selected into three groups according to their distances (0–1/3 (sector A), 1/3–2/3 (sector B), 2/3–1 (sector C) in fraction of the radius) from the center of the disk.

Other pieces of the ribbon were ball-milled (BM) in a SPEX-8000 shaker-mill, using stainless steel container and balls with a ball to material ratio of 300:1 in order to achieve high impact energy. Milling was carried out under pure argon atmosphere so as to avoid oxidation.

2.2. Microstructure

The crystalline phase analysis was carried out on diffractograms performed by a Philips (PW1130) X-ray generator with a Guinier-chamber set-up. The chamber has a diameter of 100 mm and the patterns were recorded on image plates. In this geometry samples with thickness of ~10–50 μm has been measured in transmission mode.

For high resolution transmission electron microscopy (HRTEM), the selected part of the HPT disk was prepared by twin-jet electropolishing (Tenupol-5) in a solution of water, ethanol, butoxyethanol and 1/78 ml perchloric acid (Struers A2 Electrolyte). In order to avoid the accidental artifacts during electropolishing, further cleaning of the thinned area was performed by low-angle ion milling. The thin part of the sample around the perforation was investigated in a JEOL 3010 HRTEM, operated at 300 keV.

2.3. Thermal behavior

Continuous scans at 40 K/min and isothermal heat treatments on the as-quenched ribbon, HPT disk and BM sample were carried out in a Perkin-Elmer power compensated differential scanning calorimeter (DSC), under purified argon atmosphere. The temperature and enthalpy were calibrated by using pure Al and In.

3. Results

3.1. Thermal treatments

In order to compare the crystallization products under isothermal condition with the microstructure formed after continuous heating, the as-quenched $Al_{85}Ce_8Ni_5Co_2$ alloy was subjected to isothermal heat treatments below and near T_g at $T_{ann} = 530$ K to 565 K for 30 min.

The XRD patterns in Fig. 1(a) show important changes in the microstructure of the alloy occurring during annealing. After heat treatments below T_g (between $T_{ann} = 535$ K and $T_{ann} = 540$ K) the Bragg peaks of α-Al (in the figures the fcc-Al notation specifies the structure of the precipitations) and a metastable (φ) phase appear, with a composition close to that of the relaxed matrix [34,35], meanwhile after annealing at $T_{ann} = 545$ K some new crystalline peaks emerge identified as hexagonal Al_3Ce. In Al-based metallic glasses, i.e. $Al_{90}Sm_{10}$, $Al_{91}Nd_9$, $Al_{90}Sm_8Ni_2$, $Al_{91}Ce_9$ low temperature heat treatments usually result in the nucleation of metastable phases with cubic structure [34,35]. From the peak positions the lattice parameter of the cubic φ phase can be evaluated as $a = 0{,}87$ nm. During heat treatments near T_g (above $T_{ann} = 550$ K) devitrification proceeds by the continuous transformation of the φ and Al_3Ce phases to the more stable orthorhombic $Al_{11}Ce_3$, monoclinic Al_9Co_2 and orthorhombic Al_3Ni phases.

Fig. 1(b) summarizes the effect of isothermal heat treatments on the thermal stability of the amorphous alloy. As seen continuous scans following low temperature annealing ($T_{ann} = 530$ K, 535 K, 540 K) has only a slight effect on the thermal behavior, however, heat treatments at higher temperature result in drastic change in the exothermic peak shapes. At $T_{ann} = 545$ K only the T_1 peak is affected until it totally diminishes at $T_{ann} = 550$ K. Surprisingly, scans taken after isothermal annealing between $T_{ann} = 540$ K and $T_{ann} = 547.5$ K reveal a new high temperature exothermic peak (T_3) which reaches its maximum intensity at $T_{ann} = 545$ K. As seen, $T_{ann} = 565$ K yields the total elimination of all thermal events.

The corresponding total enthalpy release (ΔH) determined from continuous heatings is shown in Fig. 1(c). No significant alteration

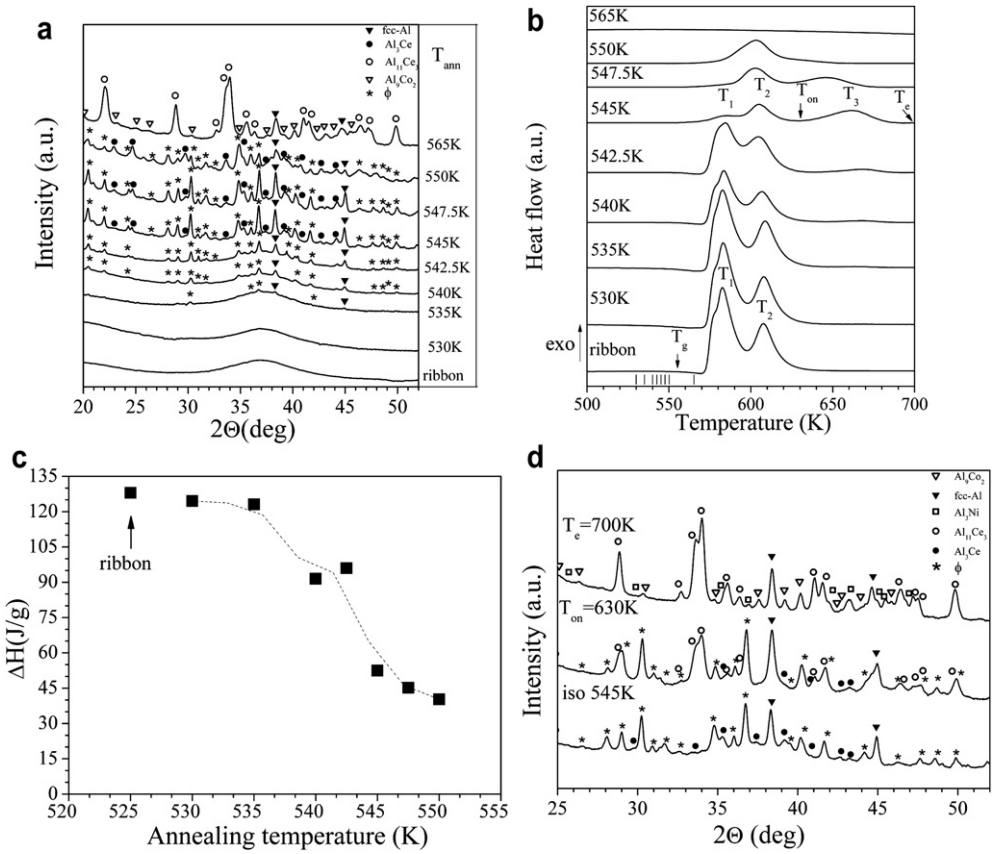

Fig. 1. XRD patterns (a) and corresponding continuous heating DSC curves (b) of as-quenched $Al_{85}Ce_8Ni_5Co_2$ alloy and samples annealed for various temperatures (T_{ann}). The T_{ann} temperatures are indicated by ticks. Changes of the total enthalpy after heat treatments as the function of annealing time (c). XRD patterns of the sample annealed at $T_{ann} = 545$ K and followed by continuous heatings up to $T_{on} = 630$ K and $T_e = 700$ K (d).

occurs until T_{ann} reaches 535 K, then a gradually decreasing tendency takes place. The slight maximum in ΔH at 542.5 K is in accordance with the appearance of the T_3 peak.

In order to reveal the microstructural changes associated with the T_3 peak, continuous heatings up to $T_{on} = 630$ K (onset of T_3 DSC peak) and $T_e = 700$ K (end of T_3 DSC peak) were carried out on the sample annealed at $T_{ann} = 545$ K, as indicated in Fig. 1(b). The corresponding XRD patterns reveals the appearance of $Al_{11}Ce_3$ at T_{on}, while a subsequent transformation of Al_3Ce and φ phases into the more stable $Al_{11}Ce_3$, Al_9Co_2 and Al_3Ni phases occurs at T_e (see Fig. 1(d)).

3.2. High pressure torsion

Figs. 2 and 3 summarize the results on the amorphous $Al_{85}Ce_8Ni_5Co_2$ alloy subjected to HPT. A HRTEM image obtained on the most deformed part of HPT disk (sector C) depicts a featureless amorphous matrix and some crystalline regions with the size of 5–10 nm (Fig. 2(a)). The periodic pattern on the filtered image (see Fig. 2(b)) and the corresponding Fourier transform (Fig. 2(c)) reveal the presence of ⟨111⟩ crystalline planes of fcc precipitations. The interplanar spacing of the precipitations has been evaluated as $d_{(111)} = 2.385 \pm 0.004$ Å, which value is approximately 2% larger than that of the fcc-Al ($d_{(111)} = 2.338$ Å).

The XRD patterns corresponding to the center of the disk (sector A) exhibits a featureless halo similarly to that of the as-quenched ribbon (see Fig. 3(a)). With increasing deformation the α-Al peaks become visible in accordance with the HRTEM image, indicating a deformation dependence of the transformed nanocrystalline fraction.

Corresponding DSC thermograms indicate that the inner regions with smaller deformation (sectors A and B) exhibit three distinct exothermic peaks (T_1, T_2, T_3), while the low temperature T_1 peak is not present in the case of sector C (see Fig. 3(b)). The total amount of heat release in the deformed regions is only somewhat smaller than that of the as-quenched alloy and it decreases with increasing deformation (Fig. 3(c)).

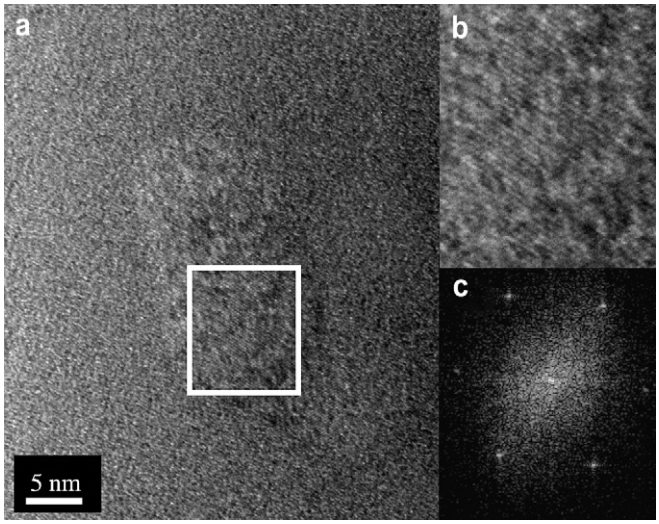

Fig. 2. HRTEM image of sector C of HPT disk (a). Fourier filtered image of the area denoted by a square (b) and the corresponding Fourier transformed diffraction pattern (c).

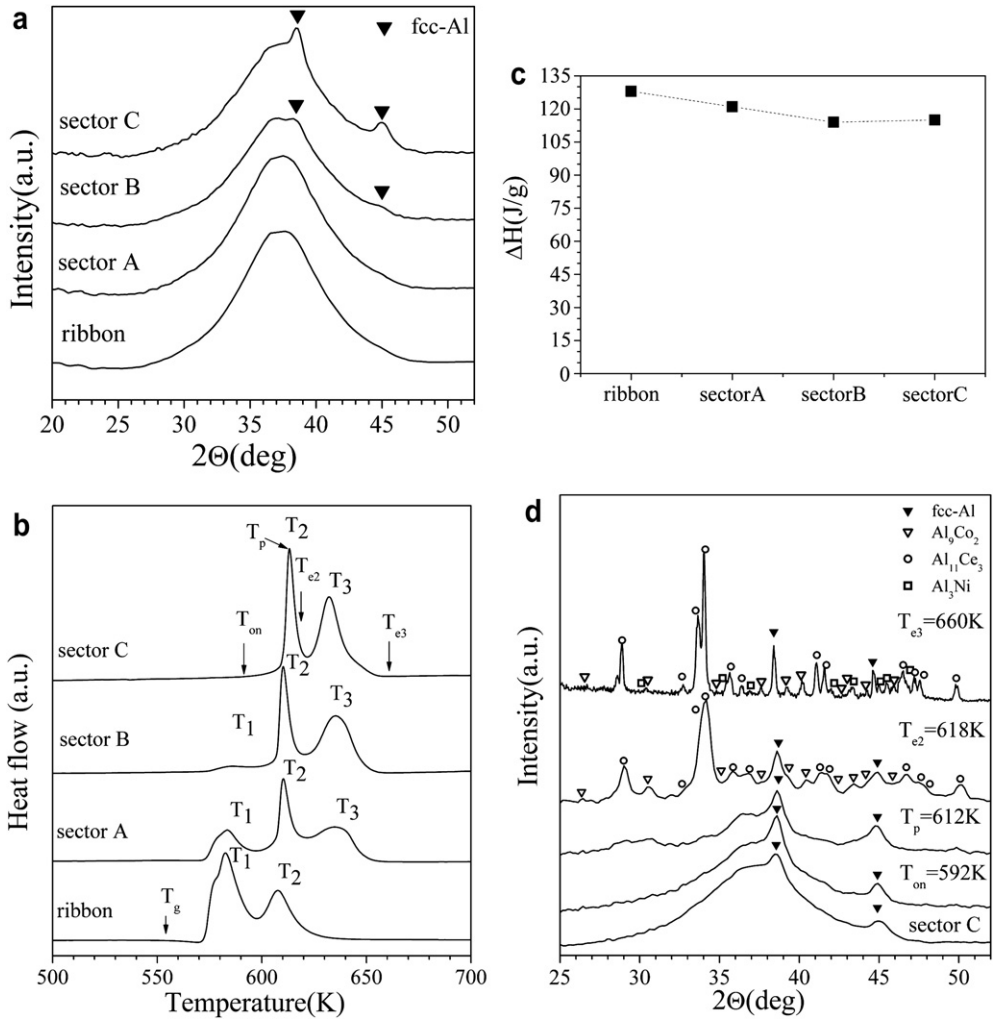

Fig. 3. XRD patterns (a) and corresponding continuous heating DSC curves (b) of as-quenched $Al_{85}Ce_8Ni_5Co_2$ alloy and that of the different sectors of HPT disk. Changes of the total enthalpy of the different sectors (c). XRD patterns taken from sector C and after continuous heatings up to $T_{on} = 592$ K, $T_p = 612$ K, $T_e = 618$ K and $T_e = 660$ K (d).

In order to characterize the high temperature behavior of the deformed state, continuous heating DSC scans were carried out on pieces of sector C up to $T_{on} = 592$ K, $T_p = 612$ K (peak temperature), $T_{e2} = 618$ K (end of T_2 DSC peak) and $T_{e3} = 660$ K (end of T_3 DSC peak), as indicated by arrows in Fig. 3(b). The corresponding XRD patterns reveal the more intensive formation of α-Al nanocrystals in the amorphous matrix at T_{on}, while the amorphous halo decomposes with the simultaneous formation of other crystalline phases at T_p (see Fig. 3(d)). The states at T_{e2} and T_{e3} exhibit the same mixture of phases (α-Al, Al_3Ce, Al_3Ni, Al_9Co_2, φ phase), the remarkable peak sharpening refers to only grain growth that takes place during the T_3 exothermic transformation of the deformed state.

3.3. Ball milling

High energy BM of the as-quenched $Al_{85}Ce_8Ni_5Co_2$ pieces was performed for durations ranging from $t_{BM} = 60$ s to $t_{BM} = 1200$ s. The XRD patterns taken after the shortest milling times up to $t_{BM} = 225$ s still reveal only the broad amorphous halo, meanwhile some sharp crystalline peaks of $Al_{11}Ce_3$ appear superimposed on the halo after $t_{BM} = 340$ s (see Fig. 4(a)). Next to the formation of $Al_{11}Ce_3$ compound the Bragg peaks of α-Al appear abruptly at $t_{BM} = 450$ s. As BM continues, the intensity of amorphous halo exhibits a decreasing tendency and it decomposes into a mixture of α-Al, $Al_{11}Ce_3$ and Al_9Co_2 after $t_{BM} = 600$ s. Prolonged milling up to $t_{BM} = 1200$ s yield no visible changes in the XRD patterns.

The corresponding continuous heating DSC curves reveal no significant changes up to $t_{BM} = 750$ s (see Fig. 4(b)). At $t_{BM} = 800$ s the intensity of the T_1 and T_2 peaks drop down simultaneously, while after $t_{BM} = 900$ s just the T_1 peak is visible and with further milling it shifts to lower temperatures and its intensity decreases. As seen in Fig. 4(c) a significant drop occurs in the ΔH value between $t_{BM} = 750$ s and 800 s, in coincidence with the offset of pulverization of the ribbon pieces in the milling vial. In order to determine the microstructural changes associated with the T_1 peak continuous heating was performed up to the end of this thermal event ($T_e = 650$ K). Subsequent XRD measurement reveals that this is a coarsening or stress relaxation process, since the Bragg peaks of pronounced crystalline phases ($Al_{11}Ce_3$, α-Al, Al_9Co_2, Al_3Ni) become sharper (Fig. 4(d)).

4. Discussion

As seen in Fig. 1(b) the as-quenched $Al_{85}Ce_8Ni_5Co_2$ amorphous alloy exhibits a two-stage thermal devitrification process

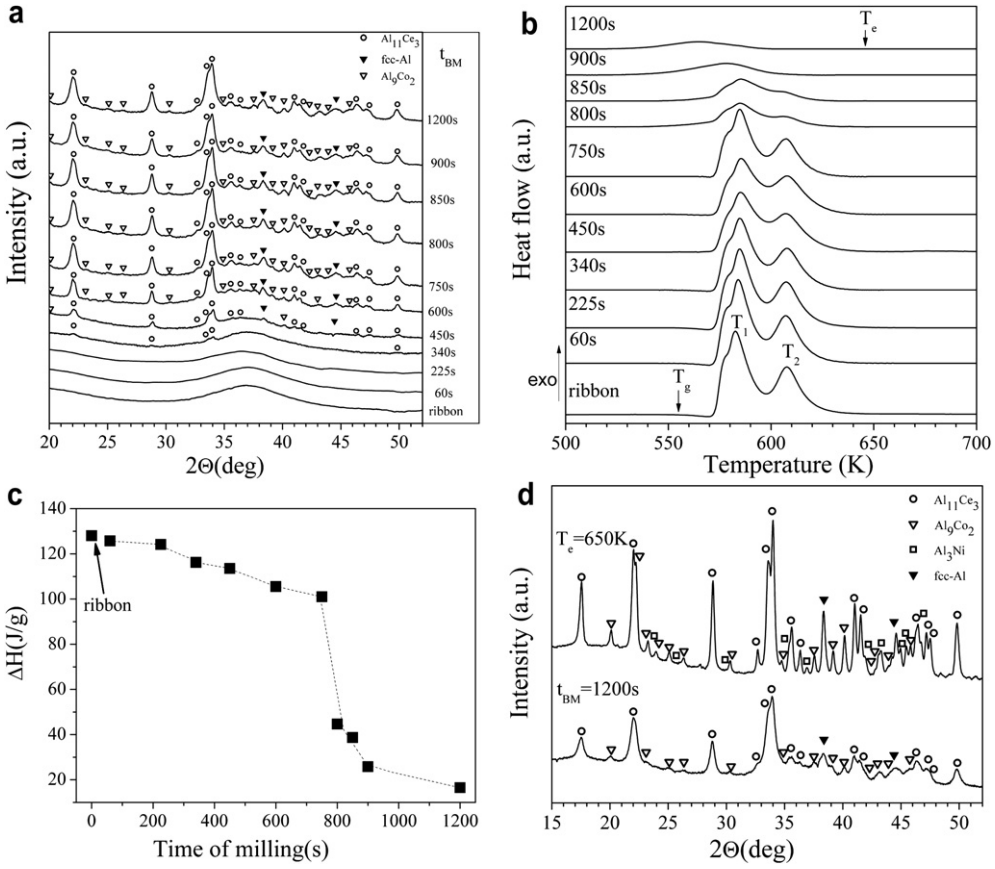

Fig. 4. XRD patterns (a) and corresponding continuous heating DSC curves (b) of as-quenched $Al_{85}Ce_8Ni_5Co_2$ ribbon and samples milled for various milling times (t_{BM}). Enthalpy changes after ball milling as a function of milling time (c). XRD patterns of the sample after ball milling for $t_{BM} = 1200$ s and after continuous heating up to $T_e = 650$ K (d).

characterized by the T_1 and T_2 crystallization peaks. Before the crystallization, the DSC thermogram also reveals a well defined glass transition, with the glass transition temperature of $T_g = 555$ K. As was shown previously, during the first transformation event (T_1) mainly α-Al, and a metastable φ phase appear simultaneously, the final microstructure, attained above T_2 contains the stable phase mixture of α-Al, $Al_{11}Ce_3$, Al_9Co_2 and Al_3Ni phases [36,37].

Applying either isothermal heat treatments or severe plastic deformation by HPT or BM (see Figs. 1(a), 3(a) and 4(a)), the first step in the devitrification of the amorphous $Al_{85}Ce_8Ni_5Co_2$ alloy can be summarized as follows:

(I.) Isothermal heat treatment: as-quenched alloy → α-Al + φ + am. matrix.
(II.) HPT: as-quenched alloy → α-Al + am. matrix.

(III.) BM: as-quenched alloy → $Al_{11}Ce_3$ + (α-Al) + am. matrix.

In general, the devitrification process can be divided into separate stages, i.e. nucleation and further growth of crystallites. The nucleation is determined by the critical thermodynamic barrier for the formation of crystalline nuclei and is governed by the driving force and interfacial free energy. Meanwhile, the growth process is mainly connected to kinetic parameters via the atomic rearrangement and transport of the partitioning atoms under different time scales. In order to clarify the differences between the crystallization sequences under various external constraints, both thermodynamic and kinetic aspects of the crystallization will be discussed hereafter.

4.1. Thermodynamics

Experimental data on off-eutectic binary Al-based amorphous alloys (Al–Gd, Al–Nd, Al–Ce) show that the thermodynamic driving force for the nucleation of α-Al increases in general with decreasing temperature [38,39]. In particular, for Al–Ce metallic glasses the driving force of $Al_{11}Ce_3$ crystalline phase formation is higher than that of α-Al close to the liquidus temperature, while at lower temperatures the nucleation of α-Al is preferred thermodynamically [40].

From the thermodynamic point of view, applied external pressure in the GPa range can have significant effect on the driving force and therefore on devitrification as well. In addition, the formation of dense, metastable crystalline phases is often preferred during the devitrification of amorphous alloys under large external pressures [41]. A detailed study on the effect of pressure on crystallization of an Al–La–Ni amorphous alloy has shown that applied pressure decreases the crystallization temperature for primary α-Al, while the crystallization of the residual amorphous phase shifts to higher temperature [42]. This phenomenon coincidences well with our experimental findings, i.e. the application of high pressures promotes primary Al crystallization (see Fig. 3(a)) as it is discussed more quantitatively in the following.

The effect of hydrostatic pressure on precipitation can be discussed within the frame of classical theory of primary, homogeneous nucleation. Simplifying the calculations, hereafter only a binary model Al–Ce alloy is considered exhibiting similar Al/Ce ratio as the experimentally investigated metallic glass. The change in the Gibbs free energy (ΔG) of the amorphous matrix associated

Table 1
Thermodynamic parameters, molar volume of the amorphous phase (V_m^a) and crystalline phase (V_m^c), interfacial free energies (σ) and thermodynamic driving forces (ΔG_m), applied in equation (2) (taken from Ref. [43]).

	V_m^a (cm^3/mol)	V_m^c (cm^3/mol)	σ (J/m^2)	ΔG_m (J/mol)
α-Al	10.7	10	0.058 $+6.69\times10^{-5}$T	8110, 345−11,034T
$Al_{11}Ce_3$	10.7	12.4	0.112 $+7.98\times10^{-5}$T	18312,26−105, 851T + 0,37T^2 − 5,765 $\times10^{-4}T^3$ + 3,967 $\times10^{-7}T^4$ − 1,004 $\times10^{-10}T^5$

with the formation of a spherical nucleus with a radius, r, can be expressed as [7]

$$\Delta G(T,P) = \frac{4}{3}\pi r^3\frac{\Delta G_m + P\Delta V}{V_m^c} + 4\pi r^2\sigma, \quad (1)$$

where V_m^c, ΔG_m and σ are the molar volumes of the crystalline phases, molar free energy difference and the interfacial free energy between the amorphous and crystalline phases, respectively, while ΔV is related to the volume change associated with the formation of crystalline nucleus and to chemical interdiffusion in the remaining amorphous matrix. Henceforward, the energy barrier per mol for nucleation (ΔG^*) required to form a nucleus with a critical size can be obtained as

$$\Delta G^*(T,P) = \frac{16\pi\sigma^3 N_A}{3}\left(\frac{V_m^c}{\Delta G_m + P\Delta V}\right)^2, \quad (2)$$

where N_A is the Avogadro number. Taking into account the relative volume change ($\Delta V/V_m^a = 1$–4%, where V_m^a is the molar volume in the amorphous phase), the pressure dependence of ΔG^* at a given temperature can be calculated for α-Al and $Al_{11}Ce_3$ based on equation (2) using the available experimental data listed in Table 1. In the case of $\Delta V/V_m^a = -2\%$ the calculated ΔG^* curves for a selected temperature ($T = 550$ K) are plotted in Fig. 5 for both phases. The intersection of the two curves defines the pressure, $\tilde{p}$, above which the formation of α-Al is more favored thermodynamically. Additional specific pressure values, corresponding to −1%, −3% and −4% of $\Delta V/V_m^a$ have also been determined. The calculated $\tilde{p}$ values for different temperatures are plotted in Fig. 6. As seen, the T–P diagram can be separated into two regions, i.e. at high temperatures the nucleation of $Al_{11}Ce_3$ is preferred because of the lower

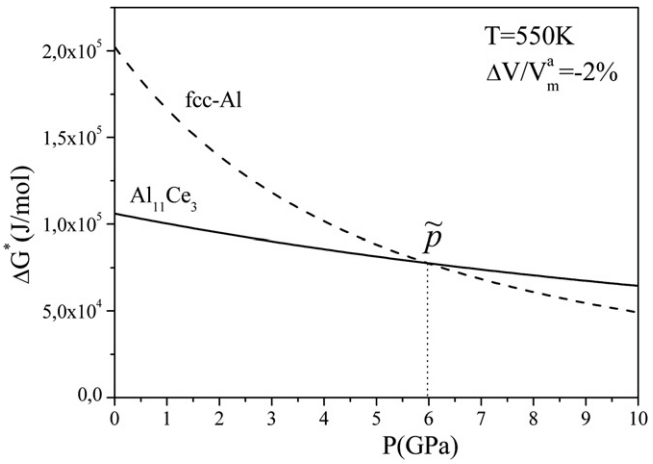

Fig. 5. Variation of energy barrier ΔG^* with the applied pressure at $T = 550$ K for α-Al and $Al_{11}Ce_3$. The intersection defines the pressure ($\tilde{p}$) above which the formation of α-Al is preferred.

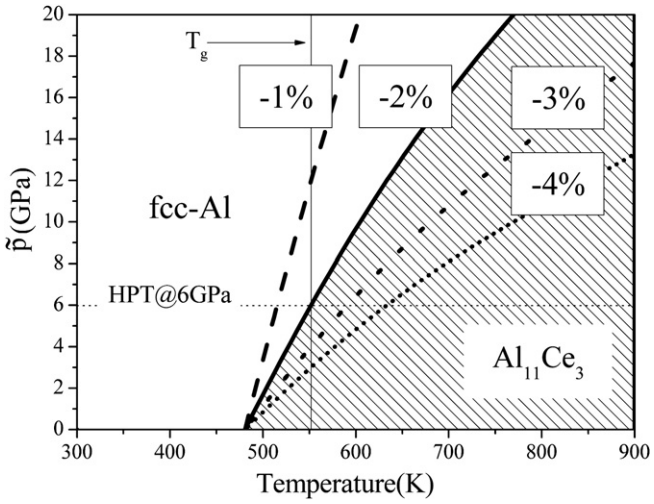

Fig. 6. Temperature-pressure phase diagram in the Al–Ce system. The curves correspond to different $\Delta V/V_m^a$. Above a critical temperature only the precipitation of $Al_{11}Ce_3$ is preferred.

nucleation barrier, meanwhile in the complementary parameter range, the nucleation of α-Al is more probable. As also seen at certain pressure values, there exists a critical temperature at 6 GPa ~600 K above which only the nucleation of $Al_{11}Ce_3$ is preferred independently of the temperature.

In order to justify the devitrification route for ball milling, local pressure and temperature can be estimated as follows. High-energy BM generates very complex stress state and plastic deformation in the powder material. Applying the model of Maurice et al. [44] based on the collisions among balls and between a ball and the vial, the impact time, strain, temperature increase in the powder and the maximum pressure developed across the contacting surfaces can be obtained. The geometry of the collision is modeled on the basis of Hertzian contacts [44]. The collisions with powder can be considered as a forging process between parallel plates leading to a maximum applied true strain

$$\varepsilon_{max} = \ln\left(\frac{h_0}{h_0 - v\tau/2}\right), \quad (3)$$

where h_0 is the initial size of powder, entrapped between colliding surfaces, v is the impact velocity of the colliding bodies (4 m/s for the SPEX mill [44]) and $2\tau = 1.25\times10^{-5}$ s is the total duration of one impact [44]. In our case h_0 can be considered as the thickness of amorphous ribbons (10–50 μm). Based on equation (3), the maximum strain in a collision is $\varepsilon_{max} = 0.25$–1.5, from which the temperature-rise under the ball can be given as [44],

$$\Delta T = \frac{\sigma_0\varepsilon_{max}}{C_p}, \quad (4)$$

where σ_0 and C_p are the yield strength the specific heat of the amorphous ribbon. With the available data for Al-based amorphous alloys ($\sigma_0 \approx 1$ GPa, $C_p \approx 2440$ kJ/(km^3) from Refs. [2] and [44]), ΔT can be estimated as 100–600 K. The local pressure developed across the contacting surfaces for the maximum compression can also be expressed from the Hertz theory as

$$p_{max} = \frac{3}{4\pi}\left(\frac{R_1+R_2}{R_1R_2}\right)^{0.5}\delta_{max}^{0.5}E_{eff}, \quad (5)$$

where R_1 and R_2 are the radii of curvature of the contacting spheres ($R_1 = \infty$ for the wall and $R_1 = 1.75$ mm, $R_2 = 3.5$ mm for the balls), $1/E_{eff} = 1/E + 1/E_{wall}$ is the effective modulus of colliding media

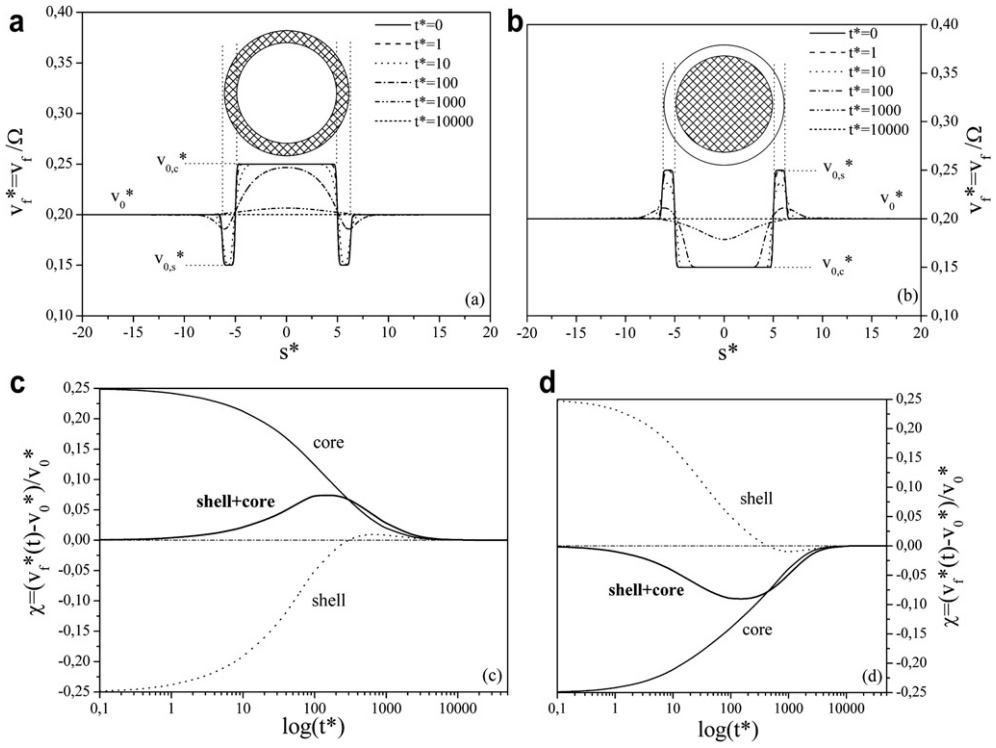

Fig. 7. Schematic illustration of a nucleated crystalline embryo and its shell and free volume, v_f^*, distribution calculated at different t^* times around a soft (a) and a dense core (b). Free volume evolution in the core and in the shell and their sum for the soft (c) and the dense core (d).

($E = 70$ GPa Al-based metallic glasses [19] and $E_{wall} \approx 200$ GPa for stainless steel) and δ_{max} is the relative displacement of the center of masses of the colliding bodies ($\delta_{max} \approx 10–20$ μm). The calculated values for the local maximum pressure are in the range of 1 GPa to 2 GPa.

The obtained values of ΔT and p_{max} for BM define a wide $P–T$ range indicating that both Al and $Al_{11}Ce_3$ can nucleate during the collisions (see Fig. 6). The relatively high temperature maximum also supports the formation of a phase mixture containing both Al and $Al_{11}Ce_3$ crystalline products which is in coincidence with the experimental results (see Fig. 4(a)).

4.2. Kinetics of crystal growth

The formation of nanocrystalline nuclei is only the first stage of the devitrification process, however, the growth kinetics of the different crystalline phases can significantly be different, even if the nucleation of one of the competing phases is thermodynamically more probable.

At temperatures around and above T_g, the atomic mobility is relatively high and can be considered homogeneous in the whole sample and is determined by the available free volume according to the theory of Doolittle [45]

$$D\left(v_f\right) = D_0 \exp\left(-\frac{\gamma\Omega}{v_f}\right). \quad (6)$$

Here $\gamma \approx 1$ and D_0 is a constant, Ω is the hard sphere size of the atom and v_f is the free volume per atom. In this temperature range the free volume and so the mobility of the free volume depend more on the actual temperature of the system than on local fluctuations of the glass. This allows continuous growth of nearly all the nucleated phases in the system irrespectively from their molar volume.

At lower temperatures ($T < T_g$), the local distribution of the free volume or the change of molar volume due to crystallization become more important and may be the key controlling parameter due to the following two reasons. First, in this temperature range, the free volume which leads to substantial atomic mobility is only available in spatially separated closed volumes [46,47]. These high mobility regions can percolate only above T_g assigning the transition to supercooled liquid state. Second, as it can be deduced from equation (6), small differences in the free volume lead to much larger relative differences in the mobility than above the glass transition temperature. Stress and/or concentration fluctuations may appear in these separated volumes (with excess free volume content) temporarily. These fluctuations can form nuclei if they become stable according to the theory of nucleation. Due to the relatively rigid structure (high viscosity) of the glass in this temperature range and the large difference between radii of the main constituents, a spontaneous concentration change in the glass always results in an internal stress (equivalent of free volume difference) which should be relaxed to form a stable nucleus. This relaxation is mainly governed by small atomic displacement, so by the equation (6) and starts immediately after instantaneous formation of a crystalline embryo or nucleus. Generally, above T_g, this is a fast process and it has no effect on the further growth of the crystallites. In this temperature range (below T_g), however, small decrease in the free volume results in substantial slow down of further redistribution.

To demonstrate this redistribution of the free volume in the nucleation process the following simple approximation is proposed. Based on atom probe concentration depth profile measurements across nuclei of partially crystallized Al–Ni–Ce alloys, Ce enriched shell around α-Al nanoparticles forms [48]. Similarly, in our model a crystalline embryo is regarded as a spherical core, while its shell contains the elements rejected during primary crystallization (see the schematic images in Fig. 7(a)

and (b)). In this approach the "free volume" term is extended to the crystalline phases as the extra volume per atom. The free volume content of the core and the shell may be significantly different after the formation of the nucleus and the deviations from the initial value can theoretically be either positive or negative based on the differences in the molar volumes of the forming crystalline phases. In order to describe qualitatively the fast spatial-temporary evolution of free volume within the core and shell, the 1-dimensional differential equation is considered:

$$\frac{\partial v_f}{\partial t} = \frac{\partial}{\partial x} D\left(v_f\right) \frac{\partial v_f}{\partial x}. \tag{7}$$

Introducing dimensionless variables, $v_f^* = v_f/\Omega$, $t^* = tD_0/a^2$, $s^* = x/a$, where a is the atomic length scale, equation (7) can be rewritten as

$$\frac{\partial v_f^*}{\partial t^*} = \exp\left(-\frac{1}{v_f^*}\right)\frac{1}{v_f^{*2}}\left(\frac{\partial v_f^*}{\partial s^*}\right)^2 + \exp\left(-\frac{1}{v_f^*}\right)\frac{\partial^2 v_f^*}{\partial s^{*2}}. \tag{8}$$

The parameters applied in equation (8) are $D_0 = 2 \times 10^{-13}$ m^2/s [49] and $a = 0.1$ nm. The initial conditions (at $t^* = 0$) are chosen as $v_0^* = 0.2$ in the matrix, $v^*_{0,c} = 1.25v_0^*$ in the core and $v^*_{0,s} = 0.75v_0^*$ in the shell. Let us consider the first order approximation when only the distribution of free volume varies, although the total amount remains unchanged, i.e. $\Delta V = 0$. The variation of v_f^* evaluated by equation (8) at different t^* times for two complementary cases, i.e. soft core and dense shell of larger $v^*_{0,c}$ and of smaller $v^*_{0,s}$ and vice versa, is presented in Fig. 7(a) and (b), respectively.

The time dependence of the relative free volume, $\chi = (v_f^*(t^*) - v_0^*)/v_0^*$, obtained by the integration of the v_f^* curves, is depicted for the soft and dense core in Fig. 7(c) and (d), respectively. As seen in Fig. 7(c), χ decreases in the core and increases in the shell, resulting in a homogenization process until the fluctuations disappear above $t^* > 8000$ for both regions. Adding the free volume content of the core and shell at each t^*, a local maximum is observed near $t^* \approx 200$, corresponding to net free volume inflow from the matrix to the nucleus (Fig. 7(c)). On contrary, a free volume outflow dominates the kinetics, for the denser core (Fig. 7 (d)). This asymmetry in the free volume redistribution between the different types of crystalline embryos is the consequence of the strong free volume dependence of the mobility at low temperatures. According to the model, the net free volume inflow and outflow determines the mobility of the system on a much longer time scale and predicts the further growth of nuclei with notably higher molar volume (i.e. smaller v_f^*) freezes in and the crystallization of only small molar volume phases is favored below the glass transition temperature. Note that if the chemical interdiffusion due to the nucleating phases occurs on a longer time scale, the local free volume is generated or annihilated, slightly modifying the term ΔV in equation (2).

The absence of $Al_{11}Ce_3$ phase in the initial step of the devitrification process of amorphous $Al_{85}Ce_8Ni_5Co_2$ during low temperature heat treatments (see Fig. 1(a)) can be explained by the kinetically blocked growth of this high molar volume phase.

5. Conclusions

Applying isothermal heat treatment, high pressure torsion and ball milling three different devitrification routes of amorphous $Al_{85}Ce_8Ni_5Co_2$ alloy have been distinguished. According to the thermodynamic nucleation barriers and the different growth rates our results can be summarized as follows:

- Low temperature heat treatment slightly below the glass transition temperature initially results in the formation of α-Al and a metastable phase (φ), Although, the nucleation of both the stable $Al_{11}Ce_3$ and Al phases are likely in this temperature range the growth of $Al_{11}Ce_3$ may be blocked due to the depletion of the free volume obtained from a 1-dimensional diffusion model. As a further devitrification product, the metastable Al_3Ce phase appears in coincidence with the appearance of a third exothermic peak in the DSC signal during continuous heating.
- Ball milling results in the formation of the stable phase mixture (including both α-Al $Al_{11}Ce_3$). This process can be considered as a high temperature heat treatment at intermediate pressures (<2 GPa).
- High pressure torsion at 6 GPa pressure results in the primary formation of α-Al nanocrystals and the appearance of a third exothermic peak similarly like the product of isotherm heat treatments which consists of α-Al, Al_3Ce and the metastable φ phase. This deformation process can be considered as a special heat treatment at low temperature ($\sim T_g$) and large pressure, possessing limited free volume fluctuations, assuring mobility for the nucleation and formation of α-Al.

Acknowledgements

We appreciate the support of the Hungarian Scientific Research Fund under grant No. F67893. The European Union and the European Social Fund have provided financial support to the project under the grant agreement no. TÁMOP 4.2.1./B-09/1/KMR-2010-0003. Á.R. is indebted for the János Bolyai Research Scholarship of the Hungarian Academy of Sciences. The authors are grateful to V. Kovács Kis for providing the HRTEM images. Zs. K appreciates the support of the Enterprise Ireland under grant "Metallic Glass Tooling for Micro Manufacturing". The authors are grateful to A.P. Zhilyaev for the HPT disk.

References

[1] Johnson WL. Prog Mat Sci 1986;30:81.
[2] Chen H, He Y, Shiflet GJ, Poon SJ. Nature 1994;367:541.
[3] Hebert RJ, Perepezko JH. Metal Mater Trans A 2008;39:1804.
[4] Lewandowski JJ, Greer AL. Nat Mat 2006;5:16.
[5] Kelton KF. Solid State Phys 1991;45:75.
[6] Debendetti PG. Metastable liquids. Princeton NJ: Princeton University Press; 1997.
[7] Ye F, Lu K. Phys Rev B 1999;60:7018.
[8] Spaepen F. Acta Metall 1977;25:407.
[9] Heggen M, Spaepen F, Feuerbacher M. J Appl Phys 2005;97:033506.
[10] Mazzone G, Montone A, Vittori Antisari M. Phys Rev Lett 1990;65:2019.
[11] Trudeau ML, Schulz R, Dussault D, Van Neste A. Phys Rev Lett 1990;64:99.
[12] Ogura A, Tarumi R, Shimojo M, Takashima K, Higo Y. Appl Phys Lett 2001;79:1042.
[13] Fan GJ, Quan MX, Hu ZQ, Löser W, Eckert J. J Mater Res 1999;14(9):3765.
[14] Gu XJ, Ye F, Zhou F, Lu K. Mater Sci Eng A 2000;278:61.
[15] Wang WH, He DW, Zhao DQ, Yao YS. Appl Phys Lett 1999;74:2770.
[16] Jiang JZ, Zhou TJ, Rasmussen H, Kuhn U, Eckert J, Lathe C. Appl Phys Lett 2000;77:3553.
[17] Lee SW, Huh MY, Chae SW, Lee JC. Scripta Mater 2006;54:1439.
[18] He D, Zhao Q, Wang WH, Che RZ, Liu J, Luo XJ, et al. J Non Cryst Solids 2002;297:84.
[19] Zhuang YX, Jiang JZ, Zhou TJ, Rasmussen H, Gerward L, Mezouar M, et al. Appl Phys Lett 2000;77:4133.
[20] Louzguine-Luzgin DV, Inoue A. J Non Cryst Solids 2005;352:3903.
[21] Jiang WH, Atzmon M. Acta Mater 2003;51:4095.
[22] Henits P, Révész Á, Zhylaev AP, Kovács Zs. J Alloys Compd 2008;461:195.
[23] Csontos AA, Shiflet GJ. Nanostruct Mater 1997;9:281.
[24] Demetriou MD, Johnson WL. Acta Mater 2004;52:3403.
[25] Tsai AP, Kamiyama T, Kawamura Y, Inoue A, Masumoto T. Acta Mater 1997;45:1477.
[26] Kovács Zs, Henits P, Zhylaev AP, Révész Á. Scripta Mater 2006;54:1733.
[27] Kovács Zs, Henits P, Zhylaev AP, Chinch NQ, Révész Á. Mater Sci Forum 2006;519–521:1329.
[28] Valiev RZ, Ishlamgaliev RK, Alexandrov IV. Prog Mat Sci 2000;45:103.
[29] Sort J, Ile DC, Zhilyaev AP, Concustell A, Czeppe T, Stoica M, et al. Sripta Mater 2004;50:1221.

[30] Boucharat N, Hebert R, Rösner H, Valiev R, Wilde G. Scripta Mater 2005;53:823.
[31] Czeppe T, Korznikova GF, Ochin P, Korznikov AV, Chinh NQ, Sypień A. J Phys Conf Ser 2008;98:062035.
[32] He Y, Poon J, Shiflet GJ. Science 1988;241:1640.
[33] Valiev RZ, Ivanisenko YV, Rauch EF, Baudelet B. Acta Mater 1996;44:4705.
[34] Rizzi P, Baricco M, Borace S, Battezzati L. Mat Sci Eng A 2001;304–306:574.
[35] Battezzati L, Baricco M, Antonione C. J Alloys Comp 1994;209:341.
[36] Révész Á, Varga LK, Suriñach S, Baró MD. J Mater Res 2002;17(8):2140.
[37] Révész Á, Heunen G, Varga LK, Suriñach S, Baró MD. J Alloys Comp 2004;368:164.
[38] Barrico M, Gaertner F, Cacciamani G, Battezzati L, Greer AL. Mat Sci Forum 1998;269–272:553.
[39] Hackenberg RE, Gao MC, Kaufman L, Shiflet GJ. Acta Mater 2002;50:2245.
[40] Barrico M, Gaertner F, Cacciamani G, Rizzi P, Battezzati L, Greer AL. Mater Sci Forum 1998;269–272:553.
[41] Ko BC, Wesseling P, Vatamanu OL, Shiflet GJ, Lewandowski JJ. Intermetallics 2002;10:1099.
[42] Ye F, Lu K. Acta Mater 1999;47:2449.
[43] Palumbo M, Papandrea C, Battezzati L. J Mater Sci 2005;40:2431.
[44] Maurice DR, Courtney TH. Mater Trans 1990;21A:289.
[45] Doolittle AK. J Appl Phys 1951;22:1470.
[46] Yang HW, Wang JQ. Sripta Mater 2006;55:359.
[47] Gao MC, Shiflet GJ. Intermetallics 2002;10:1131.
[48] Hono K, Zhang Y, Tsai AP, Inoue A, Sakurai T. Scripta Metall Mater 1995;32:191.
[49] Huang R, Suo Z, Prevost JH, Nix WD. J Mech Phys Solids 2002;50:1011.